Brain Topography
https://doi.org/10.1007/s10548-018-0668-1

ORIGINAL PAPER

Improved Back-Projection Cortical Potential Imaging by Multi-resolution Optimization Technique

Dror Haor[1,2] · Roman Joffe[1] · Reuven Shavit[1] · Ziv Peremen[2] · Yaki Stern[2] · Amir B. Geva[1,2]

Received: 15 March 2018 / Accepted: 31 July 2018

Abstract

Electroencephalogram (EEG) has evolved to be a well-established tool for imaging brain activity. This progress is mainly due to the development of high-resolution (HR) EEG methods. One class of HR-EEG is the cortical potential imaging (CPI), which aims to estimate the potential distribution on the cortical surface, which is much more informative than EEG. Even though these methods exhibit good performance, most of them have inherent inaccuracies that originate from their operating principles that constrain the solution or require a complex calculation process. The back-projection CPI (BP-CPI) method is relatively new and has the advantage of being constraint-free and computation inexpensive. The method has shown relatively good accuracy, which is necessary to become a clinical tool. However, better performance must be achieved. In the present study, two improvements are proposed. Both are embedded as adjacent stages to the BP-CPI and are based on the multi-resolution optimization approach (MR-CPI). A series of Monte-Carlo simulations were performed to examine the characteristics of the proposed improvements. Additional tests were done, including different EEG noise levels and variation in electrode-numbers. The results showed highly accurate cortical potential estimations, with a reduction in estimation error by a factor of 3.75 relative to the simple BP-CPI estimation error. We also validated these results with true EEG data. Analyzing these EEGs, we have demonstrated the MR-CPI competence to correctly localize cortical activations in a real environment. The MR-CPI methods were shown to be reliable for estimating cortical potentials, enabling researchers to obtain fast and robust high-resolution EEGs.

Keywords Multi-scaling · Cortical potential imaging · Back-projection · Optimization · Forward solution · Monte-Carlo

Introduction

Over the last decade, tremendous progress in the field of electroencephalogram (EEG) imaging has positioned high-resolution EEG as a well-established tool to image brain activity. A specific type of EEG imaging tool is cortical potential imaging (CPI). The aim of CPI is to recover the potential distribution on the cortex surface from the measured EEG on the scalp, a task is known as the *inverse problem*. Data on the underlying cortical activity is not always available from standard EEG. CPI is attractive thanks to its variety of applications that improve our understanding of the basic mechanisms of cognitive processes (Jousmäki 2000; Komssi et al. 2004; Gevins et al. 1994) to achieve better characterization of pathologies that impair normal function (Lai et al. 2011; Babiloni et al. 2006), all are connected to cortex-level brain activity. CPI and other source imaging techniques were previously used to map cortical responses underlying attention and consciousness (Sergent et al. 2005), visual processing (Roy et al. 2017), object recognition (Bar et al. 2006), motor activity (Edelman et al. 2016), and speech recognition (Ahissar et al. 2001). Furthermore, in Brodbeck et al. (2011), a study of 152 patients with epilepsy showed that EEG-based source imaging can provide higher sensitivity and accuracy than other imaging modalities, even when compared to MRI and PET.

Handling Editor: Bin He.

Electronic supplementary material The online version of this article (https://doi.org/10.1007/s10548-018-0668-1) contains supplementary material, which is available to authorized users.

✉ Dror Haor
dror.haor@gmail.com

[1] Department of Electrical and Computer Engineering, Ben-Gurion University of the Negev, Beer-Sheva, Israel

[2] ElMindA, Ltd., Herzliya, Israel

Published online: 03 August 2018

In order to maintain these highly detailed cortical potentials, many effective computational techniques have been proposed to solve the *inverse problem*. These techniques are mostly based on some type of error-function minimization. Two main approaches are available today. The first is the regularization approach (Babiloni et al. 1998; Wang et al. 1992; Pascual-Marqui et al. 1994). This type of method adds constraints to the solution in order to select a single solution from an infinite number of possibilities. The constraints involved are related to the sparsity of the solution (Ding and He 2008), the minimum energy (Hämäläinen and Ilmoniemi 1994), the minimal Laplacian matrix (Ma and Guan 2005), or the reference potential (Pascual-Marqui et al. 2011). On top of these regularization approaches, more complex methods were developed. One example is the variation and wavelet-based sparse source imaging (Zhu et al. 2014) that enforces sparsity on the solution in other domains, apart from the spatial one. Another example is the iteratively re-weighted edge sparsity minimization (Sohrabpour et al. 2016), which employs sources re-weighting to create clear edges between sources and background. These methods can be computationally efficient, but may have large errors and may not reflect the true cortical potentials due to false constraints. The second way to address such a minimization problem is to recast it as an iterative optimization one, which solves a multi-dimensional optimization process to find the global minimum. This global minimum is the cortical potential distribution that excites scalp potentials that best fit the measured EEG. Stochastic optimization algorithms, such as the genetic algorithm (GA), were found to provide sub-centimeter accuracies (McNay et al. 1996; Uutela et al. 1998), but seem to be computationally expensive due to the internal process of the algorithm and high dimensionality of the problem, that tend to be larger than 1000 (Fuchs et al. 2002). Deterministic iterative techniques such as the conjugate-gradient (CG) method (Franceries et al. 2012) or the gradient-descent (GD) method (Gevins et al. (1994) are less attractive due to the long convergence time for high-dimensionality problems. In addition, accurate and reliable results can be obtained only if the initial solution is close enough to the "actual" CPI solution, i.e., the global minimum.

These drawbacks and limits are common to all optimization schemes. In order to overcome or diminish them, the multi-resolution (MR) approach was proposed (Bendsoe and Sigmund 2013; Benedetti et al. 2008). The main idea in this scheme is to reduce the dimensionality of the problem by clustering the solution space into a few of large regions, and apply an optimization scheme to solve this problem of lower dimensionality. In the next stage, the clusters' sizes are reduced (mostly divided by two) and the process repeats itself. The initial condition for each stage is the optimized solution from the previous stage. The major advantages of the multi-resolution optimization method include: (1) topologically simple and close-to-the-global-optimum structures can be obtained without any explicit constraint, (2) a priori information can be simply exploited, and (3) the convergence is not sensitive to mathematical programming methods and yields a solution faster than regular CG or GD methods. All of these advantages make the MR an attractive optimization scheme for CPI. The MR method is used in many applications to solve the well-known inverse problem. Baussard et al. (2004) used this procedure to estimate localization and characterization of buried objects in the ground. This was done by adaptively selecting different scales of spline pyramids. Li et al. (2008) used a multi-level approach for scatterer shape reconstruction in the electromagnetic far-field based on the linear sampling method. Johnson and Xie (2011) developed a multi-scale approach to improve the segmentation of high spatial resolution images; this was performed using unsupervised techniques to evaluate segmentation quality. In addition, different methods were proposed for the optimal resolution level (Miller and Willsky 1996; Baussard et al. 2004) and regions' shapes and sizes (Céa et al. 2000; Feijóo et al. 2003). It is noted that even though the MR method is not restricted to a certain dimensionality, all of these studies were confined to two-dimensional space problems. A literature search did not uncover any prior research on the MR method to solve the CPI problem. However, in Gavit et al. (2001), the MR technique was proposed to reduce computational burden in EEG/MEG source imaging, which tries to solve for the source locations and orientations and is not using CPI that solves for the potentials within a volume without any sources.

The back projection CPI (BP-CPI) method (Haor et al. 2017) is a relatively new CPI method. The method finds a single-iterative and constraint-free solution to the Laplace equation in a realistic head model. The principle of operation is based on the fact that the CPI problem has a single solution (Yamashita 1982) when the Laplace equation has a full set of boundary conditions (BCs). The novelty of the BP-CPI method is that it estimates the inner BC using a surface Laplacian (SL) calculation and a back-projection technique, which results in a full set of BCs. Then, the Laplace equation is solved using a finite elements method (FEM)-based realistic head model. The BP-CPI method seems to be a stable and accurate method. It was rigorously validated using both simulated and experimental data and was superior to other CPI methods. The BP-CPI method is limited to the estimation of large cortical activation, due to the fact that it relies on the SL and it is very sensitive to electrode noise, which may result in large artificial activation and misinterpretation of the cortical activity map by a clinician.

In this paper, we present two novel MR-based improvements to the BP-CPI method. These optimization algorithms are used as a successive stage to the BP-CPI, and their aim is to increase its accuracy and reduce its sensitivity to noise.

The two techniques include an adaptive region clustering technique that automatically defines the regions' size and location for each optimization stage. The clusters are defined with deterministic or random processes, which result in two algorithms, denoted as the dMR and rMR, respectively. A series of Monte-Carlo simulations were carried out to validate the algorithm's performance on simulated data. Furthermore, we tested the sensitivity of the proposed methods to the change in the number of sampling EEG electrodes and different noise levels, measured on the scalp. Experimental validation was also carried out, and results for the MR-CPI methods are given relative to the BP-CPI, both are validated versus brain activity results from the literature.

Materials and Methods

Head Modeling

Van Uitert et al. (2004) have shown that realistic head modeling is crucial to maintain an accurate CPI. Here, we used realistic head geometry based on a single T1-weighted MRI scan of a subject's head. A full description of the realistic head modeling process is given in Haor et al. (2017) and will not be repeated here. In brief, the algorithm automatically segments different tissues within the MRI scan and generates a computerized head model, including conductivity values for each of the tissues. Two surfaces are of interest here—the cortex and the scalp, both are shown in Fig 1. The cortex and scalp surfaces contain 3113 and 6320 mesh nodes, denoted as N_c and N_s, respectively. In order to test the dMR and rMR as in a real clinical environment, we integrated a 128-electrode system to our head model (HydroCel Geodesic Sensor Net 128 by Electrical Geodesic. Inc.), denoted here as EGI128. We also aligned the electrodes' locations onto the scalp surface. The electrode-head alignment procedure is also given in Haor et al. (2017), and the result is shown in Fig. 1b. The alignment procedure discarded four electrodes from the EGI128 system, leaving 124 electrodes. In addition to this alignment procedure, we have also segmented the cortical surface to different functional regions of interest (ROI). The labeling of the brain regions was performed based on the automated anatomical labeling (AAL) atlas (Tzourio-Mazoyer et al. 2002). Two examples are given in Fig. 1c and d for the auditory and visual cortices, respectively. There is an overlap between the left and right primary visual cortices. This is due to differences between the AAL atlas resolution and the resolution of the T1 MRI scan used to generate the realistic head model. This overlap is minimal and does not affect the analysis.

Fast Forward Solution

Let the domain V denote the solution volume, bounded by the scalp and cortex surfaces Ω_s and Ω_c, respectively. Solving the Laplace equation (LE) for the potentials $u(r)$ in V wrapped by a constrained BCs will give the potential distribution within the solution volume. The LE formulation can be written in the form:

$$\nabla \cdot (\sigma(r)\nabla u) = 0 r \in V \tag{1}$$

$$\frac{\partial u}{\partial n} = 0 r \in \Omega_s \tag{2}$$

$$u = g r \in \Omega_c \tag{3}$$

where g is the potential distribution on the cortical surface, $\sigma(r)$ is the inhomogeneous conductivity in V, and (2) illustrates the fact that no normal current exits on the scalp surface. When applying BCs in (2) and (3), the solution is denoted as the *forward solution*. During the MR-CPI optimization process, a sequence of forward solutions is produced with the same set of finite elements, but with different g values. Thus, to perform a fast calculation for this task, the relationship between any cortical potential (CP) and its corresponding scalp potential (SP) was found. This relationship matrix is denoted as the Green's function matrix of the cortex (GFMc matrix). The relationship is expressed in Eq. (4)

$$\left[GFM_c\right] u_c = u_s \tag{4}$$

where u_s and u_c are the scalp and cortical potentials vectors, having dimensions of N_s and N_c, respectively. GFMc represents the connectivity matrix between cortical nodes' potentials and the scalp nodes' potentials. Thus, its *ith* column

(a) (b) (c) (d)

Fig. 1 Realistic head model. **a** Cortex surface, **b** scalp surface. Gray circles illustrate the locations of the electrodes, **c** primary left auditory cortex is shown in blue, and **d** primary right (red) and left (green) visual cortices, marked over the cortex surface. (Color figure online)

contains the scalp potentials excited by a spatial delta-function centered at the *ith* node on the cortical surface.

The GFMc was calculated by a series of forward solutions performed using a commercial electro-magnetic (EM) simulation software—Sim4Life 3.0 (Zurich MedTech, Zurich, Switzerland). This yields an accurate forward solution due to optimal meshing and simulation parameters defined by the software. N_c simulations were performed. In each one, an electric dipole source was placed at a distance of 5 mm, oriented normally to the cortex surface. This yields a CP distribution that is an approximation of a spatial delta-function. For each simulation, we extract the scalp and cortical potentials, denoted as u_{si} and u_{ci}, respectively. In order to correct the error in the scalp potential due to a dipole source approximation, we performed a successive second stage that transforms the scalp potentials produced by the Sim4Life to ones that correctly correspond to Eq. (4). In this second stage we built the matrix equation in (5)

$$\left[GFM_c\right] = \left[u_s^{sim}\right]\left[u_c^{sim}\right]^{-1} \tag{5}$$

where u_c^{sim} and u_s^{sim} are matrices that have u_{si} and u_{ci} as their columns, having dimensions of $[N_s x N_c]$ and $[N_c x N_c]$, respectively. This solution to (5) gives the GFMc matrix. In order to find an accurate and stable solution, u_c^{sim} must be invertible. This is accomplished by maintaining orthogonality between the matrix columns, which is the result of using superficial dipole sources as excitations for u_{ci}.

Back-Projection Cortical Potential Imaging

The BP-CPI method finds the CP estimation using a physics-based mechanism. In its essence, the algorithm solves the inverse problem by solving the LE with complementary BCs. The outer BC is the scalp potentials, which are known from the EEG measurements. The inner BC is the normal cortical current estimation. These are estimated by calculating the surface Laplacian of the scalp potentials, which is known to accurately estimate the current flowing from the skull to the scalp. Then, the algorithm uses the knowledge of the realistic head model to project these skull–scalp currents onto the cortical surface. Finally, the LE is solved using FEM, which results in the BP-CPI estimation of the CP.

Adaptive Clustering

Following the BP-CPI estimation, the proposed method performs a successive stage of MR optimization. In each stage of the optimization, the cortical surface is divided into N groups. This procedure yields an optimization process that is operating on the N-dimensional space, for each stage. In every stage of the procedure, all nodes of each group are optimized (as one) to excite the scalp potentials that will best fit the measured EEG. Then, the groups are subdivided and the process is repeated.

The initial groups are defined according to the BP-CPI as follows. First, the main peaks of the BP-CPI distribution are found. This is done by choosing all nodes that have an absolute value above a selected threshold. We defined the threshold as $\delta \cdot \max\{|u_{c0}|\}$, where u_{c0} is the initial solution and δ is selected to be 0.3. We tested different δ values varying between 0.2 and 0.5 and did not find a significant effect of these variations on the algorithm outcome. Next, a k-means clustering algorithm (Jain and Dubes 1988) is used to find the clusters' centroids and their areas. The number of clusters is defined automatically by taking the point where the percentage of explained variance (i.e., F-test) exceeds 80%. Then, the entire cortical surface is divided into groups, where the total number of groups is defined by the total cortical surface area divided by the mean cluster area found by the k-means algorithm.

In contrast to the initial grouping stage, in the next stages the groups are subdivided. Two directions are implemented for subdividing the groups. The first is a deterministic subdivision, where in each optimization stage each group of nodes is divided into two. The second direction is a random subdivision, where in each stage, smaller independent groups are created. The number of groups in the next stage is twice the number of groups in the current stage. In each stage, the regions are uniformly distributed across the cortical surface. In the random approach, to ensure better convergence, we repeat each sub-division L times and choose the best result (i.e., minimum error) before the optimization process. In both implementations, following each sub-division, the algorithm converges to the best solution that can be obtained with the current group division; then, it proceeds to the next stage where another sub-division is performed and so on, until the number of groups equals the number of mesh nodes on the cortex surface.

Figure 2 illustrates the adaptive clustering process. A deterministic and random subdivision is shown for 10, 20, and 40 regions. It can be seen that for the deterministic case, the parent-regions are the exact composition of its children-regions, whereas in the random case this is not the case. It is also seen that, in the random case, the areas of the children regions are half of their corresponding parent region.

Optimization Scheme

The entire optimization process for the dMR and rMR is shown in Fig. 2c. First, the EEG measurements are processed by the BP-CPI to estimate an initial solution. Then, the regions' numbers and their locations are determined according to the initial condition. In the next phase, the procedure divides the cortical surface into separate regions and assigns each region with a constant potential value based on

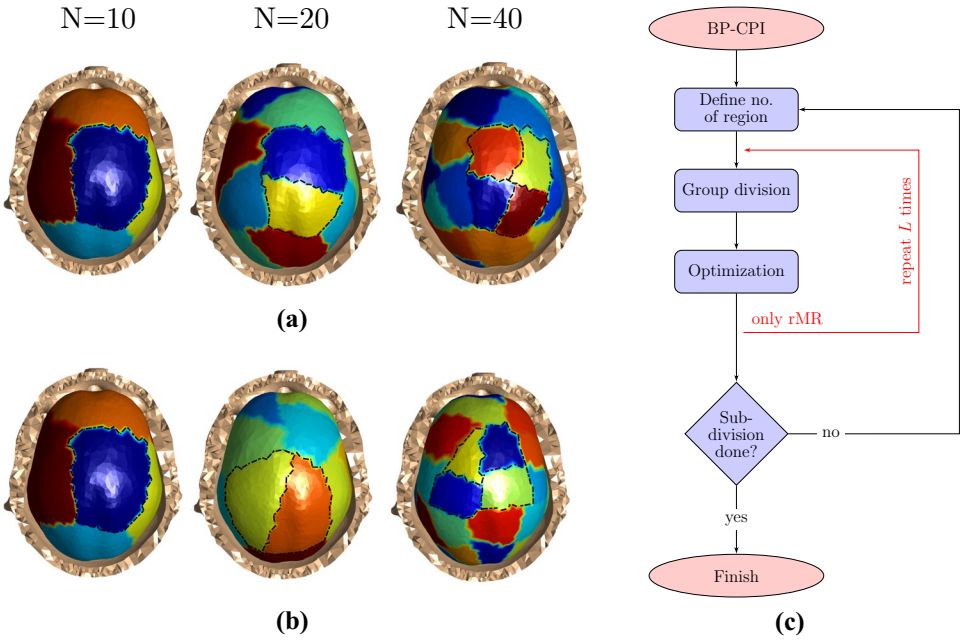

Fig. 2 Adaptive clustering and subdivision for **a** deterministic clustering and **b** random clustering. **c** The MR-CPI optimization block diagram. The dMR process is illustrated in the centerline of the diagram from top to bottom. The rMR process builds off the initial steps of the dMR process after the optimization phase through the L repetitions of group division and optimization stages

the average value in each region. Once the initial CP is determined, the first optimization stage begins. Each optimization stage comprises the following steps: (1) the forward problem is solved with the current CP estimation as g in Eq. (3). This results in the scalp potentials sampled at the electrodes' locations. (2) These calculated EEG values are compared to the measured EEG data and an error function is evaluated. (3) The error is tested versus a stage-stopping criterion. If this criterion is reached, the process moves to the next stage; if the criterion is not met, a new iteration begins within the same stage. For fast convergence, the current solution is updated by an optimal step and the process repeats until the stopping criterion is reached and the current stage concludes. For the rMR, each stage is composed of L processes of group division and optimization. Within each stage of the rMR, the group sizes are kept but their centroids are randomly displaced. This helps to avoid the local-minima problem. The value of L is empirically-defined to be inversely proportional to the number of regions where, for example, for 20 regions, L=20, and for 40 regions, L=10. In addition, for $N > 300$, random displacement of regions has a minor effect, therefor we keep L=1. When the stopping criterion has been met, the minimum-error optimized CP is selected for further processing and sub-division. (4) When the stopping criterion is reached, the algorithm determines if another sub-division can be performed. If the number of regions reached is the maximal number of regions and the solution is believed to be the global minimum, the entire process stops; otherwise, the regions are again sub-divided according to the selected scheme (random/deterministic), and another stage begins, repeating the same procedure with the current stage optimal CP estimation as input. An elaboration on the algorithm components is given next.

Error-Function

In each iteration, the error function shown in Eq. (6) is calculated,

$$J(u_c^{(i,s)}) = \left\| u_s - [GFM_c] \cdot u_c{}^{(i,s)} \right\|_2 \tag{6}$$

where u_s is the measured EEG potentials, and $\|\cdot\|_2$ is the L2 norm. The term $[GFM_c] \cdot u_c{}^{(i,s)}$ reflects the scalp potential excited at the electrodes' locations by the *ith* CP on the *sth* stage, and thus this error-function measures the difference between the measured EEG and the calculated EEG in the current iteration.

Gradient Descent and Solution Update

Within each optimization stage, the GD algorithm is used to update the solution in the direction of the global minimum. The update is done according to Eq. (7)

$$u_c^{(i,s)} = u_c^{(i-1,s)} - t^{(i,s)} \cdot \nabla J(u_c^{(i-1,s)}) \tag{7}$$

where $t^{(i,s)}$ is the update step and $J(u_c^{(i,s)})$ is the error-function evaluated for the *ith* estimated CP on the *sth* stage. We used an optimal update step, which is found using the line-search technique (Grippo et al. 1986). The optimal step is found by evaluating the error-function along a line in the direction of the error-function gradient $\nabla J(u_c^{(i-1,s)})$ and taking the minimal-error solution along the line, as depicted in Eq. (8).

$$t^{(i,s)} = \arg\min_{\alpha \geq 0} J(u_c^{(i-1,s)} - \alpha \nabla J(u_c^{(i-1,s)})) \tag{8}$$

For fast convergence, we also implemented the GD algorithm to find the optimal step along that line.

Stopping Criteria

In each stage, the algorithm tries to find the global minimum in the current N dimensions. If a close-enough solution is reached, there is no need to further converge to a better solution. Stopping the process at this point will result in a lower computation cost and shorter processing time. The MR-CPI algorithm uses a stopping criterion to detect the iteration in which a sub-division should be performed. This criterion is given in Eq. (9) and expresses the absolute directed difference between the previous iteration error function and the current one. The number of electrodes N_e is added as a normalization factor to deal with EEG measurements using a variable number of electrodes. We used $\varepsilon = 0.0005\%$

$$J(u_c^{(i-1)}) - J(u_c^{(i)}) < \varepsilon \cdot N_e \tag{9}$$

It is emphasized that, in the final stage, where the number of regions equals the number of nodes in the mesh, if Eq. (9) is reached, the algorithm ends.

Reference Simulated Data

Cortical activation is mostly composed of a number of simultaneous activations having different sizes and shapes. These can be modeled as Gaussian-pattern cortical potentials (GCP). The GCP is a three-dimensional Gaussian function as expressed in Eq. (10).

$$GCP(r) = s \cdot \exp\left((r-\mu)^T \Sigma^{-1}(r-\mu)\right)$$
$$r = \begin{pmatrix} x \\ y \\ z \end{pmatrix}, \mu = \begin{pmatrix} \mu_x \\ \mu_y \\ \mu_z \end{pmatrix}, \Sigma = diag\left(\sigma_x^2, \sigma_y^2, \sigma_z^2\right) \tag{10}$$

where r denotes the three-dimensional space coordinates, μ is the GCP peak coordinate and $\sigma_x^2, \sigma_y^2, \sigma_z^2$ are the variances of the Gaussian in the three dimensions. $diag(\cdot)$ denotes a diagonal matrix formed from its vector arguments, and s expresses the sign of the GCP. As part of the validation process, a simulated reference dataset was created. 1000 GCPs were generated by using randomized values for μ, Σ and s. μ was constrained to be on the cortical surface, Σ was kept smaller than one quarter of the cortex size in each dimension (< 30 mm), and s was randomly chosen to be 1 or -1 to maintain a normalized GCP. Following the generation of these single cortical activations, we randomly selected a combination of M GCPs from the aforementioned GCP set and combined them to generate a more complex and realistic potential distribution. 1000 combined-GCPs were generated for each selected M, where M varied between 2 and 10 combined Gaussian distributions. Thus ,when joining the single and combined cortical activations, we obtained a total of 10,000 GCPs, denoted as the GCPs dataset. These GCPs were multiplied by the GFMc matrix to generate the Gaussian-pattern scalp potentials (GSPs) dataset, which are the scalp potentials excited by the corresponding GCPs dataset.

Experimental Data

Tasks and Stimuli

We selected the visual and auditory Go-Nogo (GNG) event related potentials (ERP) tasks to validate the MR-CPI performance. These tasks are known to involve visual and auditory processing related to specific regions of the cortex : the visual and temporal cortices, respectively. In the GNG task, subjects are exposed to a series of cues and are required to react accordingly. The different cues are the 'Go' cue, in which the subjects are requested to respond as quickly as possible by pressing a keypad, and the 'Nogo' cue where the subjects are requested to inhibit their response. 80% percent of the cues are 'Go', and all others are the 'Nogo' cues, which are distributed randomly within the experiment. In the visual GNG (VGNG), the 'Go' cue stimuli are English alphabetic letters ('B', 'C', 'D', etc.) while the 'Nogo' cue stimuli is the letter 'X'. In the auditory GNG (AGNG), the 'Go' and 'Nogo' stimuli are 1000 Hz and 2000 Hz sound tones, respectively. Further description of the AGNG experimental data, experimental validation results and their interpretation are given in the supplementary materials of this article.

Subjects, Recording System and Data Preprocessing

Six participants were included in the MR-CPI experimental validation study. All subjects were healthy males, aged 25–34 years (mean = 29 years). Three participants performed a visual ERP task (VGNG) and three performed an auditory ERP task (AGNG). Scalp potentials were recorded using the 64 electrode system (BioSemi, Amsterdam, Netherlands) (10–20 layout). Basic filtering, artifact removal and trial rejection procedures were performed on the EEG raw data before averaging the ERP. In order to maintain the signal as faithfully as possible, limited filtering was performed on the signal (0.5–30 Hz BPF). This resulted in noisy signals. We quantized the noise of the signal as in Eq. (11)

$$n_{\exp} = STD_s^{BL} / RMS\{u_{scalp}\} \tag{11}$$

where STD_s^{BL} is the standard deviation of the EEG recording in the 50 ms baseline period before the onset, and u_{scalp} is the measured potential on the EEG electrodes at the component

peak time. We found that the VGNG ERPs are measured in the presence of mean noise of 12%.

ERP Components

The first negative peak, visible in the occipital electrodes of the VGNG ERPs, is denoted here as the N1v component (Fig. 3). This component's latency ranges from 100 to 200 ms and is known to be related to visual processing and detection of a visual stimulus (Luck 2014). Different studies have shown that the origin of N1v activation is the primary visual cortex (Hopf et al. 2002). The N1v wave is also sensitive to the direction of spatial attention (Hillyard and Anllo-Vento 1998), where the cortical potentials will exhibit higher activation on the contralateral side of the primary visual cortex relative to the subject attention to the stimuli. ERP signals for the subjects who performed the VGNG are denoted as ERPs1, ERPs2 and ERPs3.

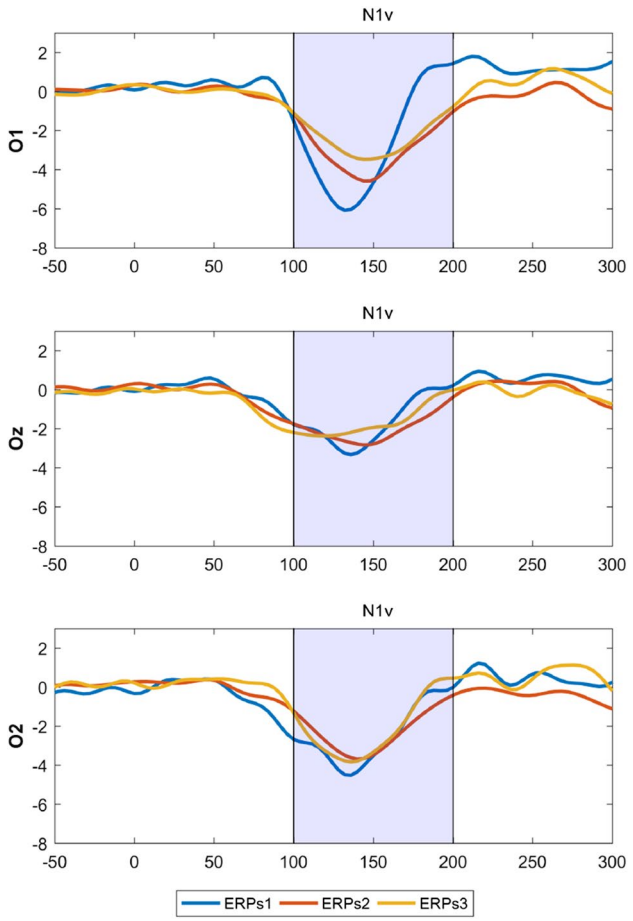

Fig. 3 Visual Go-Nogo (Go condition) ERP signals generated for different subjects. N1v component is presented from three electrodes (O1, Oz, O2) and is visible in the time range of 100–200 ms marked within the figure. Y axis is amplitude with units of [μV], and x axis is time with units of [ms]

The ERP of the AGNG was also investigated. Here, we tested the processing component which is the first negative peak of the AGNG ERP, present in the fronto-central electrodes at latencies that ranged from 80 to 120 ms. This component is denoted here as N1a. More information is given in the supplementary materials of this paper.

Cortical Potential Estimation

To validate the accuracy of the MR-CPI method, the cortical locations of the N1v and N1a were estimated. As a first step, the N1v and N1a component latencies were selected manually from the ERP. Then, potentials from 64 electrodes were used to generate CP estimations. For the visual task, the primary visual cortex is expected to be active and, for the auditory task, the primary auditory cortex is expected to be active as a bipolar (tangential) activation.

Quantitative Measures

Two measures were developed to quantitatively compare the MR-CPI improvement relative to the BP-CPI. The first measure is the *mean spread of activation* (mSOA, in mm) which is defined as the mean distance between the activation peak (A) and the contour of half amplitude (A/2). The second measure is the *relative energy* (relEN, in %) which is defined as the energy in some region relative to its surrounding regions. The mSOA is used to measure the activation focality, and the relEN quantifies the amount of activation-surrounding spatial artifacts, known to be a disadvantage of the BP-CPI.

Results

Three validation stages were applied to test the MR-CPI performance. The first included a noiseless simulation study based on Monte Carlo simulations; the second set comprised two tests, examining the effect of a noisy environment and a limited number of measurement electrodes on the algorithm's performance. The third validation stage include experimental results.

Simulation

First, we evaluated the rMR and dMR using simulated data. We adopted the Monte Carlo approach to test these algorithms for their performance in the general case. In this approach, we generated a set of reference randomly simulated inputs for the algorithm. Analyzing the distribution of the algorithm output for this random input set yielded valuable information on its performance for the general case. In our implementation, we used the GSPs dataset as the random input set. Each simulated GSP was sampled at 124 electrode positions according to the

alignment method mentioned in "Head Modeling". Then, the rMR and dMR were applied to these 124 potential values and the estimated CP was compared with the corresponding GCP (i.e., the correct CP). We used the correlation coefficient (CC) and the relative error (RE) as quantitative measures for the correctness of the estimation, as defined in Eqs. (12) and (13),

$$CC \frac{\sum_{i=1}^{N} \left(u_i^A - \bar{u}^A\right)\left(u_i^B - \bar{u}^B\right)}{\sqrt{\sum_{i=1}^{N} \left(u_i^A - \bar{u}^A\right)^2} \sqrt{\sum_{i=1}^{N} \left(u_i^B - \bar{u}^B\right)^2}} \tag{12}$$

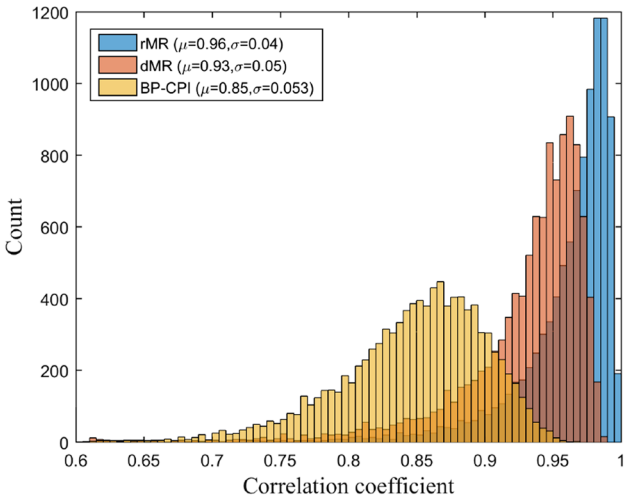

Fig. 4 Histogram representation of the Monte Carlo simulation results. The correlation coefficients for the two MR techniques are compared to the BP-CPI. Means and standard deviations are given in the legend. The difference between the groups is highly significant ($F > 10000$, $p < 1e\text{-}6$)

$$RE = \frac{1}{N} \sum_{i=1}^{N} \left| \frac{u_i^A - u_i^B}{u_i^B} \right| \tag{13}$$

where u_i^A and u_i^B are the potential values at the *ith* node of potential distributions A and B, respectively. The bar sign represents the mean of the vector, N is the total number of nodes for the potential distributions, and i includes all nodes $i = 1 \ldots N$

Figure 4 shows the histogram plot of the CC between the correct and estimated CP, for both algorithms and compared to the BP-CPI. Results show that the rMR gives the best results (mean = 0.96, SD = 0.04), the dMR shows slightly lower accuracy (mean = 0.93, SD = 0.05), but both show significant improvement relative to the BP-CPI performance (mean = 0.85, SD = 0.05). The rMR has improved the mean error of the BP-CPI by a factor of 3.75.

In addition to the Monte Carlo analysis, we have chosen two cases that showed low performance with the BP-CPI for visual inspection. Figure 5a and b show the results for the two selected distributions, denoted as distA and distB. The first includes two proximate inward oriented sources (i.e, negative GCPs) in the central part of the cortex, and an additional outward directed source in the parietal cortex (M = 3). The second case illustrates three positive activations, two in the parietal cortex and one on the left prefrontal cortex (M = 3). In both cases, the BP-CPI estimates the CP with large spatial artifacts, which results in inaccurate localization and blurring of the activation map. On the contrary to these imprecise results obtained with the BP-CPI method, the optimized cortical potentials are much more accurate,

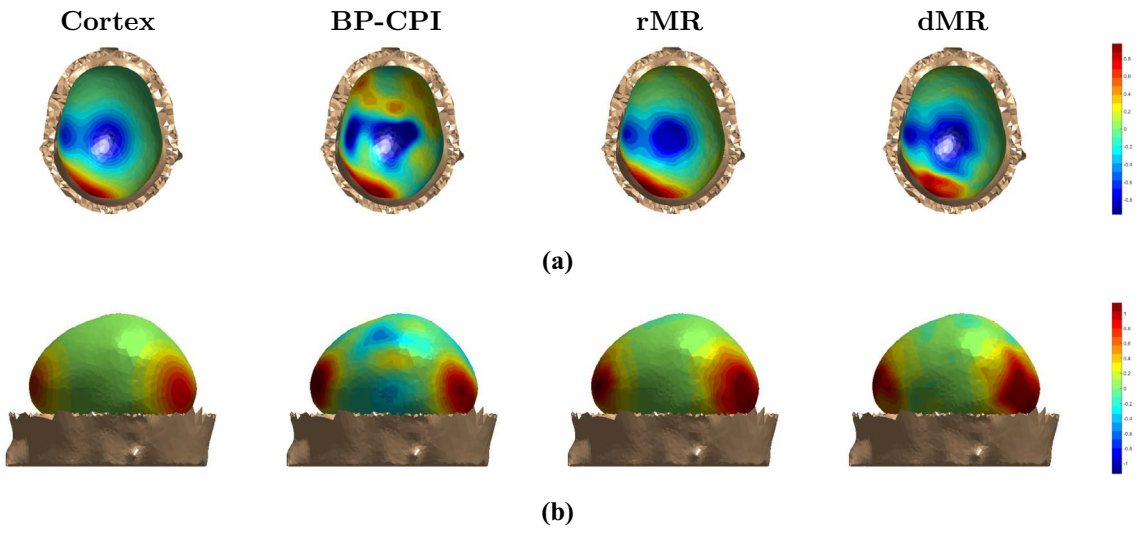

Fig. 5 Visual inspection results. From left to right: "True" cortex potential distribution, BP-CPI initial solution, rMR and dMR algorithms estimation. First and second rows corresponds to **a** distA and **b** distB, respectively. All results share the same scale

Table 1 Quantitative results for source-Gaussian model

		BP-CPI	rMR	dMR
distA	CC	0.64	0.97	0.91
	RE	0.36	0.08	0.11
distB	CC	0.53	0.91	0.87
	RE	0.26	0.04	0.09

Measures are CC/RE

with a slight advantage to the rMR method. Table 1 provides a quantitative evaluation for the accuracy of these three methods.

It is also important to investigate the convergence of these two proposed optimization methods. Figure 6a and b show the error as a function of iterations for distA and distB, respectively. The error is calculated at each iteration ($e^{(i)}$) according to Eq. (6). The convergence time for each of the proposed optimization methods can be seen. It is defined as the number of iterations calculated before the stopping criteria was achieved. In both cases, the rMR convergence time is about twice the convergence time of the dMR, however, the rMR achieves better accuracy. In addition, for the rMR, the error value spikes whenever a stage stopping criteria was achieved and clusters size was lowered. In the case of the dMR, the error in the next iteration was always smaller than the current iteration, which resulted in faster convergence time.

Sensitivity Study

Effect of Noisy EEG Measurement on MR Estimation

EEG is designed to record electrical brain activity. However, EEG measurements also include a noise component that can not be neglected. In this test, we investigated the effect of noise on the rMR and dMR CP estimation. Noises of different powers were added to the electrodes' potentials acquired from the GSP set generated for the Monte Carlo simulation presented in "Simulation" section. 500 random cases were selected. Each was sampled at 124 sites according to the EGI128 electrode set. These sampled potentials were contaminated with additive white gaussian noise (AWGN) with standard deviation (STD_{noise}), defined in Eq. (14)

$$STD_{noise} = n \cdot RMS\{u_{scalp}\} \tag{14}$$

where n is the noise level (in [%]), *RMS* is the root mean square operation, and u_{scalp} is the sampled potentials vector. Noise levels in the range of 0–30 % were tested for each of the 500 cases. Figure 7 shows quantitative measures of the effect of different noise contamination on the MR estimation. The results shows that both methods were quite robust in noise. Noise levels of 15% and below showed less than 5% decrease in estimation quality. The rMR was more robust and maintained higher mean and lower SD CC values across most noise levels. This is the result of the random property of the method that automatically finds the best regions fit for the measured EEG potentials. Figure 8 presents a visualized example of the dMR method for *distB*. Results with noise power of 10, 20 and 30% are presented. As expected, spatial artifacts are visible for higher levels of noise. However,

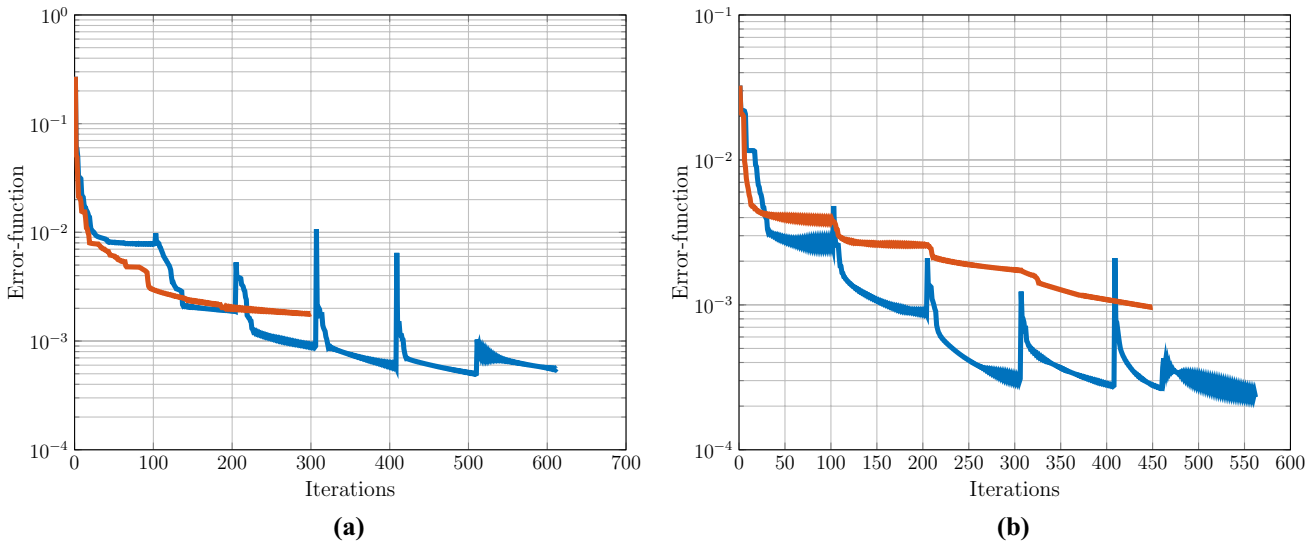

Fig. 6 Convergence time. The convergence time for **a** distA and **b** distB cases. Blue and red curves show the number of iterations for the rMR method and dMR methods, respectively. (Color figure online)

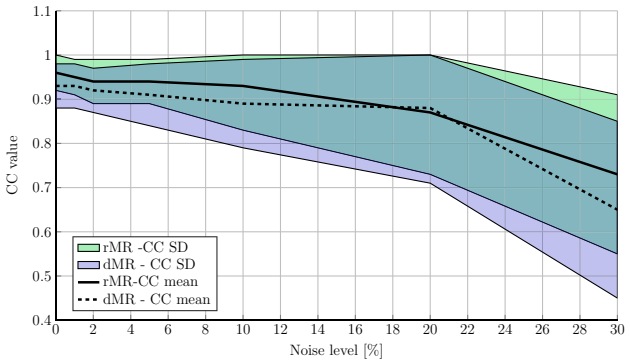

Fig. 7 MR-CPI sensitivity to electrode noise. Solid and dashed lines illustrate the mean-CC value for each noise level, for the rMR and dMR, respectively. Green and purple areas mark the CC value standard deviation for each noise level, for the rMR and dMR, respectively. (Color figure online)

the main activations are still visible even in the presence of 30% noise. The CC and RE values are also presented and show that the estimated CP shows good agreement with the original one.

Effect of Number of EEG Electrodes on MR Estimation

An EEG is only recorded at a limited number of electrodes. Thus, it is important to understand the role of this number on the quality of the estimation. In order to do so, we tested both rMR and dMR with four sizes of electrodes sets: 256, 124, 62 and 32 EEG electrodes, without adding noise. Figure 9 shows visual inspection results for distA. With 32 and 62 electrodes, the results are still blurry and do not achieve good separation of activation, whereas with 124 or 256 electrodes, the three activations are clearly seen and high CC values are achieved. In addition, 500 random cases were selected for the Monte Carlo simulation. Each was sampled at 256, 124, 64 or 32 scalp sites and the CP was estimated using both methods. Quantitative measures of the mean and standard deviation (SD) of the distribution are given in Table 2. Degradation of the estimation quality is seen for both methods, resulting in CC values of 0.86 for the worst case. When observing the results found for the 64 electrodes system, we see that the rMR method gave slightly better results compared to the dMR, reducing the RE by 15% and increasing the CC by 5%. From these sensitivity test results, we selected the rMR-CPI to be experimentally validated. 32 electrode systems are increasingly growing popular in commercial use, thus it was also interesting to test the proposed methods with this low number of sampling sites. As expected, these results show blurry CPs with lower accuracy.

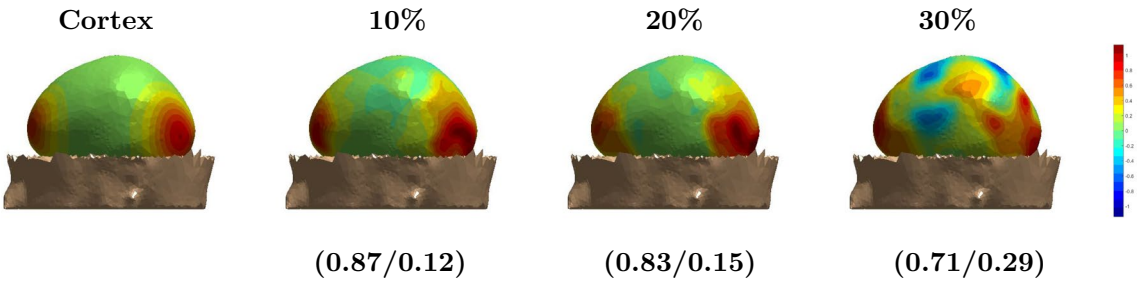

Fig. 8 The effect of noise on the dMR-CPI. From left to right—simulated CP, dMR CP estimation in the presence of 10, 20 and 30% noise levels. (CC/RE) measures are given below each plot. All results share the same scale

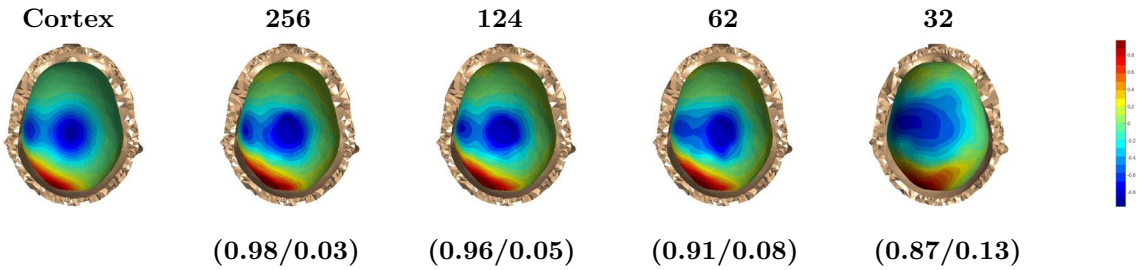

Fig. 9 The effect of EEG electrodes number on the rMR estimation. From left to right—simulated CP, rMR CP estimation using 256, 128 and 64 EEG electrodes. (CC/RE) measures are given below each plot. All results share the same scale

Table 2 The effect of number of EEG electrodes on MR estimation

		Number of electrodes			
		256	124	64	32
rMR	CC	0.98 ± 0.01	0.97 ± 0.03	0.91 ± 0.06	0.85 ± 0.09
	RE	0.04 ± 0.04	0.18 ± 0.07	0.32 ± 0.1	0.45 ± 0.17
dMR	CC	0.95 ± 0.05	0.93 ± 0.05	0.86 ± 0.1	0.82 ± 0.08
	RE	0.07 ± 0.03	0.16 ± 0.09	0.38 ± 0.23	0.53 ± 0.33

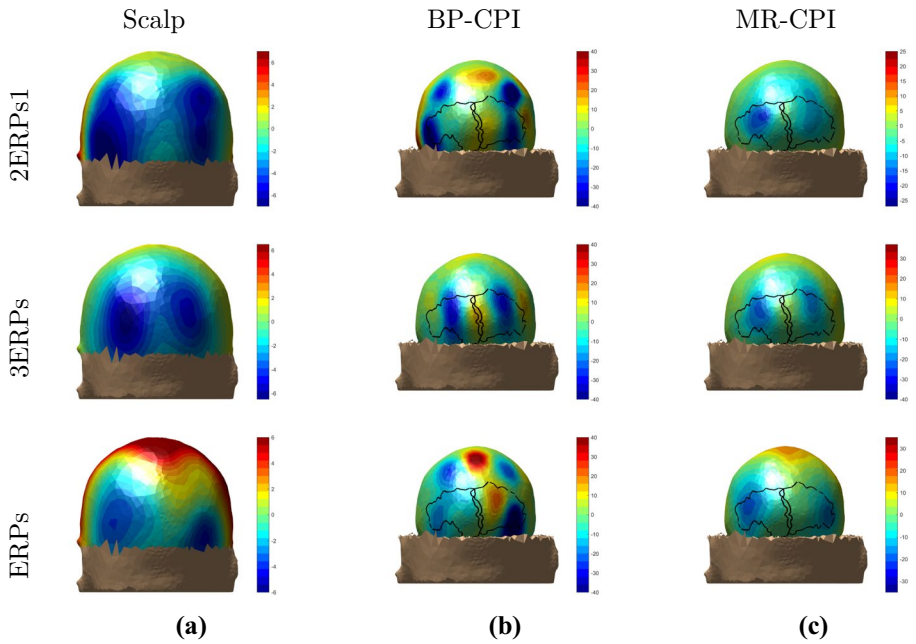

Fig. 10 Single subject results for the N1v. **a** Scalp potentials, **b** BP-CPI estimation, and **c** MR-CPI improved estimation (**c**). From top to bottom—results are plotted for ERPs1–ERPs3. The color axis is amplitude with units of $[\mu V]$. The primary visual cortex is marked in dashed lines. (Color figure online)

Experimental Results

From the rMR-CPI method, estimations of the N1v component were found in the expected cortical locations. N1v scalp potentials, along with the BP-CPI and MR-CPI estimations, are shown in Fig. 10. The "smearing" effect of the scalp potentials is clearly visible. Identifying the exact activation peak was difficult. The BP-CPI results show more focused cortical activations, but contain many spatial artifacts. The results of ERPs1 and ERPs3 show extra negative activations not located within the visual cortex. The results of ERPs2 show positive artificial activations surrounding the visual cortex-activations. These inaccurate results from the BP-CPI may corrupt the analysis. When observing the MR-CPI estimation of the N1v, symmetric activations were observed in all subjects. As expected, the activations were located within the primary visual cortex. Note that in ERPs1, the right-sided activation is weaker, which can occur when the subject is not focused at the center of the screen during the performance of the test, and thus generates higher left-sided activation. The rMR improved upon the results obtained from the BP-CPI by reducing non-true spatial artifacts and generating more focal cortical activation maps. We also compared the rMR improvement relative to the BP-CPI by using the mSOA and relEN measures, where the mSOA is given for the activation within the visual cortex region and the relEN is taken for the visual cortex relative to its surrounding regions. Results are given in Table 3. The BP-CPI does extract the visual cortex activations, although they are less focal than the MR-CPI ones. On the other hand, the relEN measure clearly shows that the BP-CPI exhibits more out-of-region spatial artifacts when compared to the MR-CPI values. These results indicate that the rMR method can localize isolated and focal cortical activation, while maintaining good spatial artifact suppression.

Table 3 Quantitative comparison between BP-CPI and rMR-CPI

	BP-CPI		rMR-CPI	
	mSOA	relEN	mSOA	relEN
ERPs1	21	30	18	352
ERPs2	38	420	12	380
ERPs3	31	76	17	210

Note that the AGNG results are given in the supplementary materials of this manuscript.

Discussion

Although several high-resolution EEG methods and cortical potential imaging algorithms are available, they exhibit several drawbacks. These drawbacks can yield errors due to false constraints taken by the method or the well-known local minima problem that can damage the solutions. In addition, good estimation techniques that maintain constraint-free accurate estimations are computationly exhaustive and are not suitable for implementation in many clinical applications.

In this study we proposed two novel improvements to the BP-CPI algorithm. These methods are based on the multi-resolution approach with random and deterministic components, denoted as rMR and dMR, respectively. The novelty of these techniques is in that they give an accurate CP while making no assumption on the number of sources nor the potential distribution or noise level. In addition, these iterative techniques adaptively converge to a correct CP estimation due to the flexible mechanism of sub-dividing regions, which fits itself to any spatial signal. The methods were evaluated using a Monte Carlo simulation approach, which gives a better understanding of the algorithm performance in the general case and not only in selected cases, as is seen in most literature reports. Three validation stages were conducted to characterize the proposed method's performance. First, a noiseless simulative study utilizing a large number of random CPs on a realistic head model showed that the mean accuracy of the methods are extremely high (CC $>$ 0.96, RE $<$ 0.1 for the rMR). These results show that the proposed improvements reduce the CP estimation error by a factor of 3.75 relative to the inaccuracy of the BP-CPI method.

The second simulation study included noisy EEG measurements and a variable number of recording sites. As expected, there is a monotonic decrease in the estimation accuracy for noisy environments. However, CC values above 0.9 were observed for noise that was 15% of the signal amplitude. The second test showed that more recording electrodes gave a better estimation. However, the difference between the results using 124 and 256 sites was negligible. These results corresponds to other source imaging and localization studies (Sohrabpour et al. 2015; Lantz et al. 2003), that showed significant accuracy improvement when sampling 124 (and more) sites compared to 64 sites. In addition, these studies showed a similar plateauing effect as seen in Table 2. In both the noise and electrode number tests, we did not find any significant advantage for one of the proposed methods over the other. Across the first two evaluation stages, the rMR had higher accuracy. This is due to the random process that is at the heart of the algorithm, which helps to maintain a close-to-global-minimum solution. Further consideration should be given for the possibility of over-fitting to noisy measurements. This research targets led us to implement this variant of the MR scheme, which has an internal "noise-filtering" process, by taking the average value of all the nodes in each region as its constant value in each stage of the optimization. Furthermore, during the study we tested for different values of ϵ in the stopping criteria. We did not find any major over-fitting effect when varying this value. It is also important to discuss the trade-off between the two proposed methods. As presented, the rMR-CPI method is more accurate than the dMR-CPI, in the general case. In addition, both methods were shown to be similarly robust to noise and the number of sampling scalp electrodes. Furthermore, the dMR calculation is faster due to convergence in less iterations, even though our implementation did not include parallel-computing, which would improve the efficiency of the rMR estimation.

According to the simulative validation results, we selected the rMR for experimental validation. Several CPI methods have shown experimental validation in the literature. He et al. (2002) have shown a good spatial correlation between the estimated and measured cortical potential for a somatosensory evoked potential (SEP). Subjects' SEPs were recorded before the subdural grid was placed on their cortex surface via surgery and compared with postoperative cortical-recorded signals. Gevins et al. (1991) showed a similar study on visual and auditory stimulation. In the present study, we also validated our method using EEG-measured signals. Due to the lack of true cortical measurements by means of functional MRI or electrocorticography (ECoG), we experimentally tested the rMR using task-based ERP signals. Six healthy subjects performed the visual and auditory Go-Nogo tasks with the aim of validating the MR-CPI. Analysis of the rMR-CPI estimation from the subjects' ERPs revealed very localized cortical activations. The visual cortex was activated during the N1v components for all subjects performing the VGNG, as expected. Compared to the BP-CPI, the MR-CPI improved the activation spread and significantly reduced the noisy cortical activation. Using the rMR we were able to separate the smeared scalp activation into two isolated occipital activations representing the visual processing activity. In addition, the location of the 'Go' cue on the subject receptive field could be detected by considering the offset of the peak activations relative to the V1 area of the visual cortex. Future analysis of these results can yield valuable information on subject visual impairment. These EEG results also emphasize the notion that the proposed method not only focuses the existing scalp potentials, but also reveals cortical activations that were unavailable when observing the scalp alone.

The results presented in this study give rise to many further research directions. Further improvements in accuracy can be achieved by modifying the initial condition. In this manuscript, we aimed at improving the BP-CPI results,

and thus used it as an initial condition to the rMR or the dMR. We can increase the accuracy or raise the stability of the solution by applying the algorithms several times with different initial conditions, such as zero or random-valued initial CP, and select the minimum-error solution. Another direction that may improve the method accuracy, mostly in experimental data, is extent imaging as in Sohrabpour et al. (2016). Extent imaging determines the active cortical region by distinguishing the desired source activity from background activity and thus, it can improve the physiological accuracy of the rMR-CPI by defining more accurately the exact source activity region. In order to generate an even more powerful clinical tool, we aim to integrate the MR-CPI with single-subject and group analysis algorithms. These can be cortical-connectivity algorithms, such as dynamic causal modeling (DCM) (David et al. 2006), or group-based scoring algorithms, such brain network activation (BNA) (Stern et al. 2016). High level analysis combined with more focused cortical potential maps can reveal brain functionality information that was not previously available to the clinician.

Acknowledgements This work was supported (in part) by Grant from the MAGNET program of the Israeli OCS and by ElMindA Ltd.

References

Ahissar E, Nagarajan S, Ahissar M, Protopapas A, Mahncke H, Merzenich MM (2001) Speech comprehension is correlated with temporal response patterns recorded from auditory cortex. Proc Natl Acad Sci 98(23):13367–13372

Babiloni C, Frisoni G, Steriade M, Bresciani L, Binetti G, Del Percio C, Geroldi C, Miniussi C, Nobili F, Rodriguez G et al (2006) Frontal white matter volume and delta eeg sources negatively correlate in awake subjects with mild cognitive impairment and alzheimer's disease. Clin Neurophysiol 117(5):1113–1129

Babiloni F, Carducci F, Babiloni C, Urbano A (1998) Improved realistic laplacian estimate of highly-sampled eeg potentials by regularization techniques. Electroencephalogr Clin Neurophysiol 106(4):336–343

Bar M, Kassam KS, Ghuman AS, Boshyan J, Schmid AM, Dale AM, Hämäläinen MS, Marinkovic K, Schacter DL, Rosen BR et al (2006) Top-down facilitation of visual recognition. Proc Natl Acad Sci USA 103(2):449–454

Baussard A, Miller EL, Lesselier D (2004) Adaptive multiscale reconstruction of buried objects. Inverse Probl 20(6):S1

Bendsoe MP, Sigmund O (2013) Topology optimization: theory, methods, and applications. Springer, Berlin

Benedetti M, Lesselier D, Lambert M, Massa A (2008) A multi-resolution technique based on shape optimization for the reconstruction of homogeneous dielectric objects. Inverse Probl 25(1):015009

Brodbeck V, Spinelli L, Lascano AM, Wissmeier M, Vargas MI, Vulliemoz S, Pollo C, Schaller K, Michel CM, Seeck M (2011) Electroencephalographic source imaging: a prospective study of 152 operated epileptic patients. Brain 134(10):2887–2897

Céa J, Garreau S, Guillaume P, Masmoudi M (2000) The shape and topological optimizations connection. Comput Methods Appl Mech Eng 188(4):713–726

David O, Kiebel SJ, Harrison LM, Mattout J, Kilner JM, Friston KJ (2006) Dynamic causal modeling of evoked responses in eeg and meg. NeuroImage 30(4):1255–1272

Ding L, He B (2008) Sparse source imaging in electroencephalography with accurate field modeling. Hum Brain Mapp 29(9):1053–1067

Edelman BJ, Baxter B, He B (2016) Eeg source imaging enhances the decoding of complex right-hand motor imagery tasks. IEEE Trans Biomed Eng 63(1):4–14

Feijóo GR, Oberai AA, Pinsky PM (2003) An application of shape optimization in the solution of inverse acoustic scattering problems. Inverse Probl 20(1):199

Franceries X, Chauveau N, Sors A, Masquere M, Celsis P (2012) Conjugate gradient method applied to cortical imaging in eeg/erp. In: Petrova R (ed) Finite volume method-powerful means of engineering design. InTech, Rijeka

Fuchs M, Kastner J, Wagner M, Hawes S, Ebersole JS (2002) A standardized boundary element method volume conductor model. Clin Neurophysiol 113(5):702–712

Gavit L, Baillet S, Mangin JF, Pescatore J, Garnero L (2001) A multiresolution framework to meg/eeg source imaging. IEEE Trans Biomed Eng 48(10):1080–1087

Gevins A, Le J, Brickett P, Reutter B, Desmond J (1991) Seeing through the skull: advanced eegs use mris to accurately measure cortical activity from the scalp. Brain Topogr 4(2):125–131

Gevins A, Le J, Martin NK, Brickett P, Desmond J, Reutter B (1994) High resolution eeg: 124-channel recording, spatial deblurring and mri integration methods. Electroencephalogr Clin Neurophysiol 90(5):337–358

Grippo L, Lampariello F, Lucidi S (1986) A nonmonotone line search technique for newtons method. SIAM J Numer Analy 23(4):707–716

Hämäläinen MS, Ilmoniemi RJ (1994) Interpreting magnetic fields of the brain: minimum norm estimates. Med Biol Eng Comput 32(1):35–42

Haor D, Shavit R, Shapiro M, Geva A (2017) Back-projection cortical potential imaging: theory and results. IEEE Trans Med Imaging 36(7):1583–1595

He B, Zhang X, Lian J, Sasaki H, Wu D, Towle V (2002) Boundary element method-based cortical potential imaging of somatosensory evoked potentials using subjects' magnetic resonance images. NeuroImage 16(3):564–576

Hillyard SA, Anllo-Vento L (1998) Event-related brain potentials in the study of visual selective attention. Proc Natl Acad Sci 95(3):781–787

Hopf JM, Vogel E, Woodman G, Heinze HJ, Luck SJ (2002) Localizing visual discrimination processes in time and space. J Neurophysiol 88(4):2088–2095

Jain AK, Dubes RC (1988) Algorithms for clustering data. Prentice-Hall Inc, Englewood Cliffs

Johnson B, Xie Z (2011) Unsupervised image segmentation evaluation and refinement using a multi-scale approach. ISPRS J Photogramm Remote Sens 66(4):473–483

Jousmäki V (2000) Tracking functions of cortical networks on a millisecond timescale. Neural Netw 13(8):883–889

Komssi S, Huttunen J, Aronen HJ, Ilmoniemi R (2004) Eeg minimum-norm estimation compared with meg dipole fitting in the localization of somatosensory sources at s1. Clin Neurophysiol 115(3):534–542

Lai Y, Zhang X, van Drongelen W, Korhman M, Hecox K, Ni Y, He B (2011) Noninvasive cortical imaging of epileptiform activities from interictal spikes in pediatric patients. Neuroimage 54(1):244–252

Lantz G, De Peralta RG, Spinelli L, Seeck M, Michel C (2003) Epileptic source localization with high density eeg: how many electrodes are needed? Clin Neurophysiol 114(1):63–69

Li J, Liu H, Zou J (2008) Multilevel linear sampling method for inverse scattering problems. SIAM J Sci Comput 30(3):1228–1250

Luck SJ (2014) An introduction to the event-related potential technique. MIT press, Cambridge

Ma X, Guan X (2005) Loreta-contracting algorithm for solving eeg source distribution problems. COMPEL-Int J Comput Math Electr Electron Eng 24(3):821–828

McNay D, Michielssen E, Rogers R, Taylor S, Akhtari M, Sutherling W (1996) Multiple source localization using genetic algorithms. J Neurosci Methods 64(2):163–172

Miller EL, Willsky AS (1996) A multiscale, statistically based inversion scheme for linearized inverse scattering problems. IEEE Trans Geosci Remote Sens 34(2):346–357

Pascual-Marqui RD, Michel CM, Lehmann D (1994) Low resolution electromagnetic tomography: a new method for localizing electrical activity in the brain. Int J Psychophysiol 18(1):49–65

Pascual-Marqui RD, Lehmann D, Koukkou M, Kochi K, Anderer P, Saletu B, Tanaka H, Hirata K, John ER, Prichep L et al (2011) Assessing interactions in the brain with exact low-resolution electromagnetic tomography. Philos Trans R Soc Lond A 369(1952):3768–3784

Roy AV, Jamison KW, He S, Engel SA, He B (2017) Deactivation in the posterior mid-cingulate cortex reflects perceptual transitions during binocular rivalry: evidence from simultaneous eeg-fmri. NeuroImage 152:1–11

Sergent C, Baillet S, Dehaene S (2005) Timing of the brain events underlying access to consciousness during the attentional blink. Nat Neurosci 8(10):1391

Sohrabpour A, Lu Y, Kankirawatana P, Blount J, Kim H, He B (2015) Effect of eeg electrode number on epileptic source localization in pediatric patients. Clin Neurophysiol 126(3):472–480

Sohrabpour A, Lu Y, Worrell G, He B (2016) Imaging brain source extent from eeg/meg by means of an iteratively reweighted edge sparsity minimization (ires) strategy. NeuroImage 142:27–42

Stern Y, Reches A, Geva AB (2016) Brain network activation analysis utilizing spatiotemporal features for event related potentials classification. Front Comput Neurosci 10:137

Tzourio-Mazoyer N, Landeau B, Papathanassiou D, Crivello F, Etard O, Delcroix N, Mazoyer B, Joliot M (2002) Automated anatomical labeling of activations in spm using a macroscopic anatomical parcellation of the mni mri single-subject brain. Neuroimage 15(1):273–289

Uutela K, Hamalainen M, Salmelin R (1998) Global optimization in the localization of neuromagnetic sources. IEEE Trans Biomed Eng 45(6):716–723

Van Uitert R, Johnson C, Zhukov L (2004) Influence of head tissue conductivity in forward and inverse magnetoencephalographic simulations using realistic head models. IEEE Trans Biomed Eng 51(12):2129–2137

Wang JZ, Williamson SJ, Kaufman L (1992) Magnetic source images determined by a lead-field analysis: the unique minimum-norm least-squares estimation. IEEE Trans Biomed Eng 39(7):665–675

Yamashita Y (1982) Theoretical studies on the inverse problem in electrocardiography and the uniqueness of the solution. IEEE Trans Biomed Eng 11:719–725

Zhu M, Zhang W, Dickens DL, Ding L (2014) Reconstructing spatially extended brain sources via enforcing multiple transform sparseness. NeuroImage 86:280–293